Understanding the mechanical strength and dynamic structural changes of wood-based products using X-ray computed tomography

Wanzhao Li[1,2], Zheng Zhang[2], Changtong Mei[1,2], Pierre Kibleur[3], Joris Van Acker[2,3],Jan Van den Bulcke[3]

[1]*Co-Innovation Center of Efficient Processing and Utilization of Forest Resources, N anjing Forestry University, Longpan Road 159, 210037 Nanjing , China*

[2]*College of Materials Science and Engineering, Nanjing Forestry University, Longpan Road 159, 210037 Nanjing, China*

[3]*UGCT-UGent-Woodlab, Laboratory of Wood Technology, Department of Environment, Faculty of Bioscience Engineering, Ghent University, Coupure Links 653, 9000 Ghent, Belgium*

Understanding the mechanical strength and dynamic structural changes of wood-based products using X-ray computed tomography

Abstract:

In service, the mechanical strength of wood-based products (WBP) is determined by the anatomical structure of wood, including the specificities of earlywood (EW) and latewood (LW), and the bonding interphase between wood and adhesive. In this study, two-layered specimens were manufactured according to three possible assembling strategies in terms of anatomical structure of wood. Wood micro-structure and phenol-formaldehyde (PF) adhesive distribution were visualized with optical and fluorescence microscopy. Internal structure changes were dynamically monitored using X-ray computed micro-tomography (X-ray μCT) while compressing specimens. The results showed that in EW, adhesive can penetrate into cell-lumens through collapsed cell-walls. In LW, adhesive can diffuse along rays. In a bonding interphase consisting of EW and LW, adhesive preferably penetrated into EW. The presence of adhesive increases EW stiffness, but has little impact on the stiffness of LW. During compression, EW was mainly compressed due to the collapse of the thinner cell-walls and larger lumina. Collapse of the cell-walls was more likely to happen in regions close and parallel to the boundary of growth rings. The cell structure in regions adjacent to resin ducts of LW was more affected, as these can be squeezed under compression.

Keywords: *Anatomical structure; Adhesive；Structural changes; X-ray computed tomography*

1. Introduction

Wood is increasingly used in load-bearing applications in construction, which naturally benefits from using fast growing softwood species. However, to reach the desired mechanical properties with a rather lightweight re-engineered wood product, it is often processed into wood based products (WBP). WBP, such as plywood, laminated veneer lumber and oriented strand boards (OSB), consist of veneers or sawn timber bonded together with adhesive. Hence, the mechanical performance of WBP is determined by wood and adhesive, as well as the interphase between wood and adhesive. Adhesive is a bridge that connects the independent wood pieces; adhesive penetration into the porous network of wood cells can impact the mechanical performance of WBP (Li et al. 2020a). The impact of wood species, wood defects, adhesive types, hot pressing techniques and wood-treatment technologies on the mechanical performance of WBP has been investigated. Jin et al. (2014) recognized that thermal modification can improve the dimensional stability and mechanical properties of WBP. Furthermore, higher knot proportion and lathe-check intervals in veneers result in a decrease of the modulus of elasticity (MOE) and modulus of rupture (MOR) of laminated veneer lumber (Purba et al. 2019). Both bending strength and splitting strength of WBP closely relate to the type and amount of adhesive (Ozkaya et al. 2013). In addition to wood and adhesive, hot-pressing techniques have also been reported to strongly affect the physical and

mechanical performance of WBP (Wang et al. 2005). Al-though extensive studies have been conducted, the interaction between the adhesive and the wood and how it affects mechanical performance is still unclear. It is therefore necessary to investigate the effect of the anatomical structure of wood, bonding interphase and their interactions on the mechanical performance of WBP. Because in service, WBP are likely to support loading charges, it is particularly relevant to investigate the micro-structural changes and mechanical performance of WBP in dynamic compression experiments.

Wang, et al. (2016, 2019) found that phenol formaldehyde (PF) can not only fill cell-lumens, but also can penetrate into the cell-walls, which can improve the stiffness and dimensional stability of wood. For softwood-based WBP, the adhesive distribution and mechanical strength closely relate to the typical wood anatomy, i.e. earlywood (EW) and latewood (LW) (Biblis and Chiu 1972; Cramer et al. 2005). X-ray computed micro-tomography (X-ray μCT) has proven to be an effective tool to visualize the internal structure of wood-based composites (Li et al. 2016; Choi et al. 2017). Since the grey scale value (GSV) of X-ray μCT data linearly relates to density, density profiles of wood-based materials could be obtained from X-ray μCT (Li et al. 2013). Furthermore, X-ray μCT enables mapping internal structure changes and density profiles of wood-based composites, in a set-up that monitors the specimen (semi-) continuously. Li et al. (2020c) have used X-ray μCT to investigate the dynamic internal structure changes of OSB under dynamic compression conditions.

The objective of this study was to systematically investigate the mechanical performance of WBP by simultaneously monitoring compressive strength (CS), adhesive distribution and internal structure changes. The relation between internal structure changes and CS was explored. Understanding the interaction of the wood micro-structure, the adhesive distribution and the CS, is paramount to optimize WBP manufacturing strategies, helping the effective use of WBP in load bearing applications.

2. Material and Methods

2.1 Preparation of specimens

Wood blocks, located around two meters above ground and the 18th growth ring counting from the pith, were cut from a Douglas fir (*Pseudotsuga menziesii (Mirb.) Franco*) stem harvested in China. As such, the impacts of juvenile wood were eliminated from the specimens. Wood density was approximately 530kg/m^3 after conditioning at a temperature of 20°C and 65% relative humidity (RH). Wood blocks measured 100×10mm² in cross-section, area with a thickness of 2.8mm. Two-layered panels were prepared, using a panel press. The following hot-pressing parameters were used: phenol formaldehyde (PF) adhesive amount of 150 g/m^2, temperature of 140°C, compressive strength of 1.2 N/mm^2 during 20 min. PF adhesive with 64% solid content was purchased from a Dynea adhesive company. Wood

blocks were arranged so that the grain directions was parallel. Considering the superposition of two wood blocks containing EW and LW, three possible assembling strategies were realized: EW/EW (E|E), LW/EW (L|E) and LW/LW (L|L) (Fig.1). Once assembled, a specimen measuring 4.0×4.0×5.0 mm was carefully cut and selected from each type of panel. Wood anatomy in two sides of the bonding interphase can fit the requirements of assembling strategies in small specimens. High resolution CT images can also be obtained using small specimens. The three specimens were conditioned at 20°C and 65% RH, for 4 weeks.

Figure1

2.2 Microscopic measurements

Cross-sections, 5mm×3mm×20μm (length×width×thickness) were cut from two layered panels with a microtome (REM-710, YAMATO, Japan), and then stained with 0.05wt% toluidine blue for 5min to depress light from lignin, and then were washed and dehydrated using 30wt% ethyl alcohol for 20 min (Shi et al. 2021). The cross-sections were then covered by a coverslip that were sealed with glycerin. The microstructure of wood was observed using an optical microscope equipped with a UV-light source (BX51, OLYMPUS, Japan). An exciter-barrier filter set (excitation wavelength 330~400 nm, emission wavelength 425 nm) was chosen to observe the adhesive distribution.

2.3 X-ray CT scanning under dynamic loading conditions

Three specimens measuring 4.0×4.0×5.0mm set in a compression stage, were scanned at different time intervals with a high-energy CT scanner (HECTOR) optimized for research, developed by the UGent Centre for X-ray tomography (Masschaele et al. 2013) controlled by a LabVIEW® based software platform (Dierick et al. 2010). A single scan was optimized to run within 25 min, and a voxel pitch of approximately 12 μm was obtained. All tomographic reconstructions were performed using the software package Octopus Reconstruction (Vlassenbroeck et al. 2007), licensed by TESCAN XRE (www.XRE.be, part of the TESCAN ORSAY HOLDING a.s.).

The specimens were positioned in a custom-made specimen holder, and compressed using a CT5000 tensile stage (Deben Ltd., United Kingdom) (Li et al. 2020b). This load cell can be controlled by displacement (±0.001 mm), or by loading force (±0.1 N). A first scan was acquired to record the specimens in their original condition. A loading force of 20.0 N (1.25 N/mm^2 compressive strength) would correspond to a specimen state free from macro- or microscopic deformations, and could therefore be used as reference. Subsequently, the specimens were scanned at three other compression steps that were determined by constant displacement of the load cell jaws. The steps at 0.5 mm, 1.0 mm and 2.0 mm were set based on prior testing. In this case, the specimens were compressed at four compression steps in total, further referred to as step-0, step-1, step-2 and step-3. The speed of the load cell jaws was limited to be as slow as possible: 0.1 mm/min. After reaching the targeted displacement, the load-cell jaws were blocked, and the scans were started after a 10 min stall. This delay is

helpful to prevent motion artifacts that would otherwise be inherent to the relaxation of the specimen's microstructure.

2.4 Data processing

The thickness of the cell-walls and the diameter of cell-lumens were measured from the optical microscopy images. Double cell-wall thickness was measured and used in data analysis. The diameter of cell-lumens was measured along the tangential direction. Sixty cells in EW and LW each, were randomly selected and their dimensions were measured. Moreover, in ten positions of each side of the bonding interphase, the maximum adhesive-penetration depth was measured on the fluorescence microscopy images. All these measurements were manually performed using ImageJ (Schneider et al. 2012).

Therefore, the distribution of GSVs was considered an appropriate proxy for the density distribution. The GSVs in a region of interest (ROI; yellow rectangles in Fig.1) adjacent to the boudline were selected for analysis. Slice by slice in the thickness direction, the GSV was calculated. The GSV data was further corrected by getting rid of the GSV of air according to:

$$G_i=GR_i-GA_i \quad (1)$$

Where G_i is GSV in a slice of ROI at compression step i, GR_i is average GSV in a slice of ROI before calibrating at compression step i and GA_i is average GSV of air in a slice of the ROI at compression step i.

To label the changes induced by compression as a function of wood anatomy, specimens were divided into EW and LW regions by thresholding the GSV or density (Antony et al. 2012). This is indicated in Fig.1. For instance, the E|E specimen was divided into four parts, namely LW-1 (L1), EW-1 (E1), EW-2 (E2) and LW-2 (L2). The thickness of each part was measured from the X-ray CT images. Then, the decrease in thickness of each part throughout compression was calculated using Eq. 2. Furthermore, the porosity in each part was calculated after manually separating air and wood based on their big GSVs difference of the X-ray CT images.

$$D_i=(T_0-T_i)/T_0 \quad (2)$$

Where D_i is the decrease in thickness in one part at compression step-i (%), T_0 is the thickness in one part at compression step-0 (mm) and T_i is the thickness in one part at compression step-i.

The CS of a specimen at one compression step was calculated according to Eq. 3. The contact area at different compression steps was measured on X-ray CT images.

$$CS_i=F_i/S_i \quad (3)$$

Where CS_i is the compressive strength of a specimen at compression step-i (N/mm^2), F is the loading force applied on a specimen at compression step-i (N) and S_i is the contact area between a specimen and the loading jaws at compression step-i (mm^2).

3. Results and discussion

3.1 Wood micro-structure and distribution of adhesive in the bonding interphase

The wood micro-structure conditions the penetration of adhesive, and therefore WBP's macro-properties. The dimensions of sixty cells in both EW and LW were measured in optical microscopy images. Cell-wall thicknesses and lumen diameters qualitatively follow normal distributions, as seen in Fig. 2. The double thickness of cell-walls in EW and LW are 2.4±0.6 μm and 8.5±2.1 μm, respectively. The average diameter of cell-lumens, measured in the tangential direction in EW and LW, are 38.9±11.4 μm and 7.8±4.1 μm, respectively. Thick cell-walls can enhance wood stiffness, and limit adhesive penetration into the cell (Walker 2006). In practice, the mechanical performance of WBPs can be improved by taking advantage of specific EW and LW properties within the bonding interphase.

Figure2

Three possible assembling strategies, i.e. E|E, L|E and L|L, were evaluated by measuring the maximum penetration depth of adhesive on fluorescence microscopy images. Adhesive-penetration behaviour is commonly evaluated with the value of the maximum penetration depth (Kamke and Lee 2007). Fig. 3 reveals that the adhesive penetration depth difference in two sides of a bonding interphase is not substantial, provided the wood anatomical structure is identical on both sides. Adhesive penetration in EW was considerable deeper than in LW, if both phases are present at the interphase. The large amount of adhesive accumulates in cell-lumens of EW, resulting in small amount of adhesive accumulation and shallow adhesive penetration through LW in the L|E specimen. However, the average adhesive penetration depth in the L|L specimen is higher than in the E|E specimen, which could be due to their different penetration strategies. Adhesive moves along the paths with least resistance, while the microstructure disparity between EW and LW shall differentiate the adhesive penetration strategies. Combining the wood microstructure in optical microscopy images and adhesive distribution in fluorescence microscopy images, can found that adhesive penetrated LW rays preferentially, while it largely accumulated in cell-lumens of EW (Fig. 4). During hot pressing, hydrodynamic flow is the dominating factor to adhesive-penetration in wood (Kamke and Lee 2007). Adhesive was able to flow along cell-lumens in the longitudinal direction. Hence adhesive appears in cell-lumens isolated from the bond-line, perhaps because the tracheids are not perfectly parallel to the bond-line. Cell-lumens next to the bond-line have the least resistance to liquid flow, therefore adhesive obviously accumulates in these regions. However, no evidence of adhesive penetrating even the thinner cell-walls was found. Adhesive penetration in cell-lumens is possible along the ruptured cell-wall, caused by high pressure or cutting during specimen preparation. Cell-walls in EW are thin and prone to collapse during hot pressing, while the thicker cell-walls in LW do not. The cell-wall of fourth tracheid counted from the bond-line onwards (highlighted with a red rectangle in Fig. 4) was ruptured in EW, while the morphology of the second tracheid from the adhesive line was almost intact in LW. Therefore, adhesive can only move along rays if both sides of the bonding interphase are LW. Indeed, adhesive can hardly move through the cell-lumens of LW.

Furthermore, rays are oriented normal to the plane of bond-line, thus adhesive prefers to diffuse along rays in LW (Jakes et al. 2019). Hence, adhesive penetrates deeper along rays in LW than along cell-lumens in EW.

Figure3

Figure4

3.2 Mechanical performance of specimens

The CS of specimens is likely determined by the wood anatomy, as can be seen in Table 1. The E|E specimen has a larger CS than both the L|L and L|E specimens. This is due to the high LW ratio in the E|E specimen. Although the specimens were carefully selected to assure a similar wood anatomy at the two sides of the bonding interphase, the LW ratio in the three specimens was not controlled to be consistent. In comparison to EW, LW has a high density, which is proportional to the mechanical strength of wood (Wang et al. 2018a). From the evolution of the CS in function of time, it could be observed that significant changes only occur in step-3. This is because the decrease in thickness through steps 1 and 2 is mainly caused by the collapse of cells with large cell-lumens. The CS in all three specimens is therefore comparable, as long as the EW is not collapsed. Based on the X-ray CT images, it was found that the internal structure changes relate to proportion and location of EW and LW, as well as assembling strategies (Fig.5). For instance, for L|L specimen, collapse profile in EW closely relates to the profile in LW. To further understand these phenomena, regional density, porosity and micro-structure changes were studied.

Table1

Figure5

Apart from LW|EW ratios, different assembling strategies affect adhesive diffusion and stress transfer during compression. To further understand the impact of adhesive diffusion and the internal structure changes throughout compression were investigated. Density changes, analogous to the GSV profiles, were calculated within the manually extracted ROIs (Fig.6). We found that density in regions adjacent to adhesive lines changes little throughout compression, which means that the presence of adhesive can enhance the mechanical strength of wood. This is due to the possible PF penetration into cell-walls, which can enhance mechanical properties of wood cell-walls (Wang et al. 2018b). Meanwhile, adhesive penetration can reduce stress concentration at the bonding interphase (Frihart 2005). Cell-lumen saturation also positively relates to the bonding strength (Hass et al. 2012), which could also contribute to the stiffness increase in EW. The influence of adhesive on the mechanical strength of LW is however limited. Obviously, LW is already quite stiff and the presence of minor amounts of adhesive in LW cell-walls can hardly contribute to an increase

in stiffness. EW in the ROIs is significantly compressed in E|E, while this phenomenon is less clear in L|E (Fig.6). It could be due to the large volume of EW in the L|E specimen (table 1), which avoids stress concentrations, and conditions local thickness changes. At step-3, although EW thickness is further decreased, thickness decrease in LW starts to appear (Fig.6). Hence, LW ratio is an important factor of decrease in thickness at step-3.

Figure6

The decrease in thickness of each region defined in Fig.1 confirms that the decrease in thickness in EW determines the thickness of the specimen (Fig.7). The decrease of LW thickness was small in all three specimens. In the same specimen, the compression of EW is not homogeneous, especially at step-1 and step-2. For instance, the decrease in thickness in the E1 and E2 regions of the L|E specimen are 43.8% and 9.1% at step-2, respectively. This disparity decreases at step-3: 62.5% and 40.1%, respectively. The cell-wall thickness and lumen diameter can affect this decrease under compression. Cell-wall provides strength to lead to stress transferal and prevent structural changes during compression. Lumen space is likely to deform, which contributes to specimens' elasticity and structural rupture. The location of EW and LW, can also influence the structural changes of specimens under compression. However, a more detailed analysis on the structural changes is required.

Figure7

3.3 Structural changes of specimens under compression

After thresholding, the evolution of porosity in each region can be monitored through compression (Fig.8). Low porosity is equivalent to high density, which corresponds to small decrease in thickness under compression. For the L|E specimen, E2's porosity is lower than E1's at step-0. Therefore, the decrease in thickness in E1 is larger than in E2 (Fig.7). At step-2, the decrease in thickness in E2 is still small even though the porosity in E2 becomes even lower than in E1. Cell collapse can occur in regions with thin cell-walls or high porosity, even at the compression onset. Porosity in these regions is then reduced by compression. Eventually, it is even more likely to get increased compression or decrease in thickness in these regions due to cell-wall collapse. Indeed, in comparison to an intact cell-wall, the stiffness of a collapsed cell-wall is low (Zhang et al. 2010). This analysis can also be used to explain the behavior of E1 and E2 in the L|L specimen. At step-3, porosity in the EW is even lower than in LW. However, the decrease in thickness still mainly occurs in EW, which further concurs our analysis.

In LW, porosity hardly changes, including small decrease and even slight increase. (Fig.8). Porosity could decrease further due to the squeezing of cell-lumens and resin ducts. Porosity increase is probably caused by the occurrence of cracks. Due to the high stiffness of LW, stress can be effectively transferred to regions with lower stiffness. It increases stress concentration, and the emergence of cracks in these weak spots.

Figure8

To understand the mechanical performance of specimens under compression, it is very informative to visualize the structural changes. Fig.9 confirms that structural changes mainly occur in EW, as opposed to LW. Cell collapse in EW is particularly prominent in regions delimited by dashed red lines in Fig.9. These lines are close to, and approximately parallel to the growth ring between LW and EW. Cell collapse in EW could be due to the stress concentration in those regions with abrupt structural differences. Consistent results were reported by Li, et al. (2020b). They found that fracture planes were nearly parallel to the growth rings in poplar under compression. During compression, stress transfers from LW to EW. LW can effectively transfer stress due to its high stiffness. Therefore, EW would be compressed according to the shape of LW.

Figure9

Structural changes are initiated in the EW, and propagate to LW. We find that structural changes in LW are not obvious until EW cells are entirely collapsed (top row in Fig.10). The structural changes in LW are more likely to occur in resin ducts instead of cell-lumens. At step-3 two resin ducts, indicated with arrows in Fig.10, are squeezed. The structural changes are squeezing of the resin ducts whether or not combined with emerging cracks. For this resin duct with emerging cracks, a ray traverses the duct. The structure of the ray is therefore broken following squeezing of the resin duct. This results in a large crack. This observation matches that LW fibers tend to separate rather than collapse, as opposed to those in EW (Law 2006). However, structural changes of rays are not substantial when they do not cross through resin ducts. Based on the above analysis, we find that the sequence of structural changes in LW starts with squeezing of the resin ducts, which is followed by fracture of rays, and cell-lumen collapse. Decrease in thickness in LW shown in Fig.7 is dominated by squeezing of resin ducts and ray fracture. Porosity increases in LW, reported in Fig.8, resulted from the emergence of cracks.

Figure10

4. Conclusions

The micro-structure of wood, the adhesive distribution at the bonding interphase, and dynamically recorded internal structure changes of three specimens during compression were investigated. It was found that the assembling strategy strongly impacts the adhesive distribution at the bonding interphase. In a latewood/earlywood (L|E) specimen, adhesive is likely to penetrate farther in earlywood (EW) than in latewood (LW). In a latewood/latewood (L|L) specimen, adhesive penetrates LW mainly via rays. However, adhesive can also penetrate along cell-lumens through collapsed cell-walls, which was not found in LW. The presence of adhesive can enhance the stiffness of EW, while having little influence on the

stiffness of LW. A decrease in thickness occurred in EW, because of cell-wall collapses. Thin cell-walls were prone to collapse. The structural changes in EW started in regions parallel to the boundary of growth rings. Instead, structural changes in LW were minimal, due to the thicker cell-walls and higher stiffness. Structural changes in LW occurred only when the EW structure was entirely compacted. Structural changes in LW were mainly found in regions adjacent to the resin ducts. Resin ducts could be squeezed under compression. If there are rays across the resin duct, it is possible to cause large cracks. Based on these results, it could conclude that adhesive distribution at the bonding interphase closely relates to the micro-structure of wood. Wood anatomical features such as EW and LW, and how they are positioned in WBP, can have a significant influence on WBP mechanical performance. Therefore, findings of this study can contribute to the design of manufacturing strategies aimed at increasing the CS of WBP.

Acknowledgements

This study was financially supported by National Key R&D Program of China (2021YFD2200602) and the Postgraduate Research&Practice Innovation Program of Jiangsu Province (SJCX21_0333). The authors thank the Research Foundation – Flanders (FWO) for funding author Pierre Kibleur within the MoCCHa-CT project (S003418N). The authors would like to thank Mr. Iván Josipovic for technical assistance.

References:

Antony F, Schimleck LR, Daniels RF (2012) A comparison of earlywood-latewood demarcation methods-A case study in Loblolly Pine. IAWA journal/ International Association of Wood Anatomists 33,187–195

Biblis EJ, Chiu YS (1972) Gluability of Loblolly pine earlywood and latewood. Wood Fiber

Choi BY, Himmi SK, Yoshimura T (2017) Quantitative observation of the foraging tunnels in Sitka spruce and Japanese cypress caused by the drywood termite Incisitermes minor (Hagen) by 2D and 3D X-ray computer tomography (CT). Holzforschung 71,535–542

Cramer S, Kretschmann D, Lakes R, Schmidt T (2005) Earlywood and latewood elastic properties in Loblolly pine. Holzforschung 59,531–538

Dierick M, Van Loo D, Masschaele B, Boone M, Van Hoorebeke L (2010) A LabVIEW® based generic CT scanner control software platform. Journal of X-ray Science and Technology 18,451–461

Frihart CR (2005) Adhesive bonding and performance testing of bonded wood products. Journal of Astm International 2,12

Hass P, Wittel FK, Mendoza M, Herrmann HJ, Niemz P (2012) Adhesive penetration in beech wood: experiments. Wood Science & Technology 46,243–256

Jakes JE, Frihart CR, Hunt CG, Yelle DJ (2019) X-ray methods to observe and quantify adhesive penetration into wood. Journal of Materials Science 54,705–718

Jin HK, Shin RH, Ayrilmis N, Han TH (2014) Properties of solid wood and laminated wood lumber manufactured by cold pressing and heat treatment. Materials & Design 62,375–381

Kamke FA, Lee JN (2007) Adhesive penetration in wood-a review. Wood and Fiber Science 39,205–220

Law K (2006) The nature of mechanical failure of earlywood and latewood in software. pp 26–34

Li W, Zhang Z, Zhou G, Mei C (2020a) Understanding the interaction between bonding strength and strain distribution of plywood. International Journal of Adhesion and Adhesives 98

Li W, Van den Bulcke J, De Windt I, Dhaene J, Van Acker J (2016) Moisture behavior and structural changes of plywood during outdoor exposure. European Journal Of Wood And Wood Products 74,211–221. https://doi.org/10.1007/s00107-015-0992-z

Li W, Van den Bulcke J, De Windt I, Van Loo D (2013) Combining electrical resistance and 3D X-ray computed tomography for moisture distribution measurements in wood products exposed in dynamic moisture conditions. Building & Environment 67,250–259

Li W, Zhang Z, Zhou G, Kibleur P, Mei C, Shi J, Van Acker J, Van den Bulcke J (2020b) The effect of structural changes on the compressive strength of LVL. Wood Science & Technology 54,1253-1267

Li W, Chen C, Shi J, Mei C, Kibleur P, Van Acker J, Van den Bulcke (2020c) Understanding the mechanical performance of OSB in compression tests. Construction & Building Materials 119837

Masschaele B, Dierick M, Van Loo D, Boone MN, Brabant L, Pauwels E, Cnudde V , Van Hoorebeke L (2013) HECTOR: A 240kV micro-CT setup optimized for research. Journal of Physics: Conference Series 463,012012

Ozkaya K, Ayrilmis N, Dizel T, Ozgur Imirzi H (2013) Utilization of extract of fresh tree leaves as extender in synthetic adhesives for laminated veneer lumber (LVL). Industrial Crops & Products 44,67–70

Purba CYC, Pot G, Viguier J, Ruelle J, Denaud L (2019) The influence of veneer thickness and knot

proportion on the mechanical properties of laminated veneer lumber (LVL) made from secondary quality hardwood. European Journal of Wood and Wood Products 77,393-404

Schneider CA, Rasband WS, Eliceiri KW (2012) NIH image to ImageJ: 25 years of image analysis. Nature Methods 671–675

Shi J, Xia C, Peng J, Liu X, Pan B (2021) Cellular and Metabolite Changes in the Secondary Phloem of Chinese Fir (Cuninghamia lanceolata (Lamb.) Hook.) during Dormancy Release. Forests 11:1552

Vlassenbroeck J, Dierick M, Masschaele B, Cnudde V, Van Hoorebeke L, Jacobs P (2007) Software tools for quantification of X-ray microtomography at the UGCT. Nuclear Instruments & Methods in Physics Research 580,442–445

Walker JCF (2006) Primary wood processing: principles and practice

Wang BJ, Dai C, Dai C (2005) Hot-pressing stress graded aspen veneer for laminated veneer lumber (LVL). Holzforschung 59,10–17

Wang J, Xuan W, Zhan T, Zhang Y, Lv C, He Q, Fang L, Lu X (2018a) Preparation of hydro-thermal surface-densified plywood inspired by the stiffness difference in “sandwich structure” of wood. Construction & Building Materials 177,83–90

Wang X, Chen X, Xie X, Cai S, Yuan Z, Li Y(2019) Multi-scale evaluation of the effect of phenol formaldehyde resin impregnation on the dimensional stability and mechanical properties of Pinus Massoniana Lamb. Forests 10,646

Wang X, Deng Y, Li Y, Kjoller K, Roy A, Wang S (2016) In situ identification of the molecular-scale interactions of phenol-formaldehyde resin and wood cell walls using infrared nanospectroscopy. Rsc Advances 6:10.1039.C6RA13159J

Wang X, Zhao L, Deng Y, Deng Y, Li Y, Wang S (2018b) Effect of the penetration of isocyanates (pMDI) on the nanomechanics of wood cell wall evaluated by AFM-IR and nanoindentation (NI). Holzforschung 72,301–309

Zhang X, Zhao Q, Wang S, Trejo R, Lara Curzio E, Du G (2010) Characterizing strength and fracture of wood cell wall through uniaxial micro-compression test. Composites: Part A 41,632–638

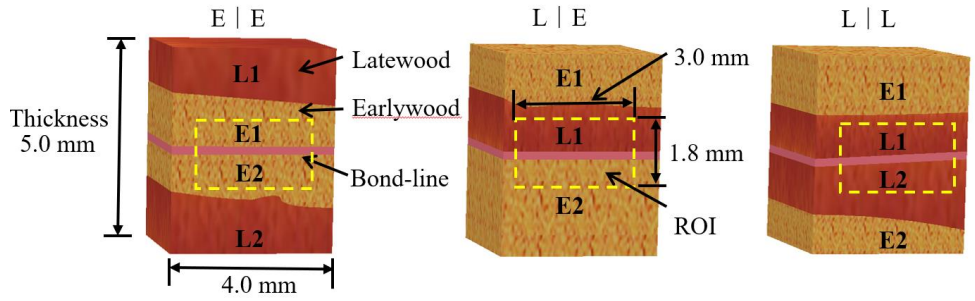

Fig.1. Assembling strategies and wood anatomy information of three specimens. (E=earlywood, L=latewood, ROI= region of interest)

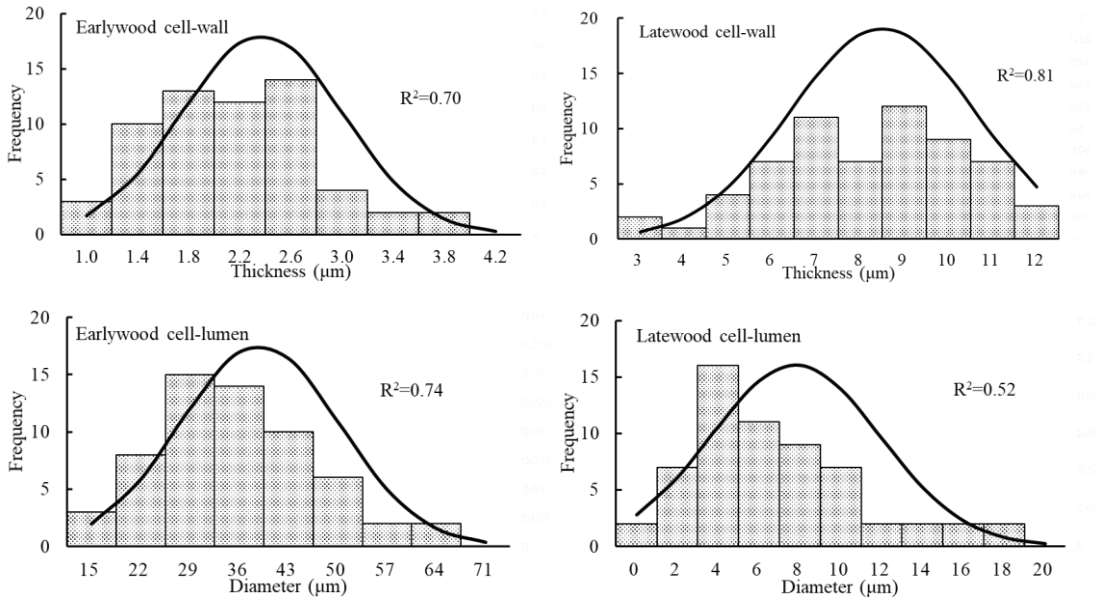

Fig.2. Distribution of cell-wall thickness and cell-lumen diameter in earlywood and latewood. R2 indicates the correlation between actual and normal distribution.

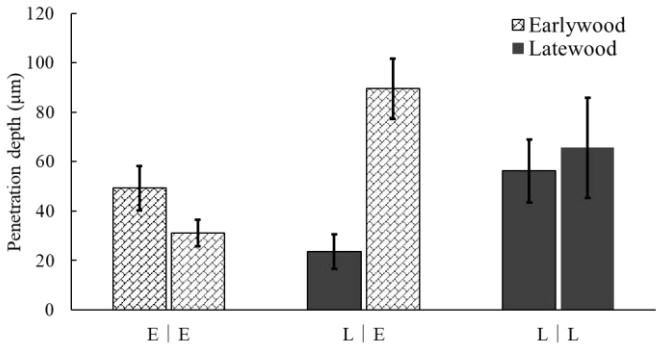

Fig.3. The maximum adhesive penetration depth in two sides of bonding interphase of three specimens.

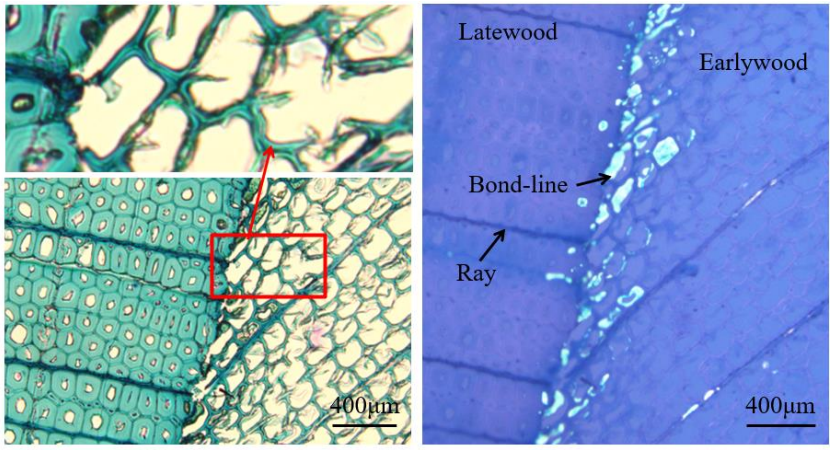

Fig.4. Cross-section views showing wood micro-structure (left) and adhesive penetration(right)at the bonding interphase.

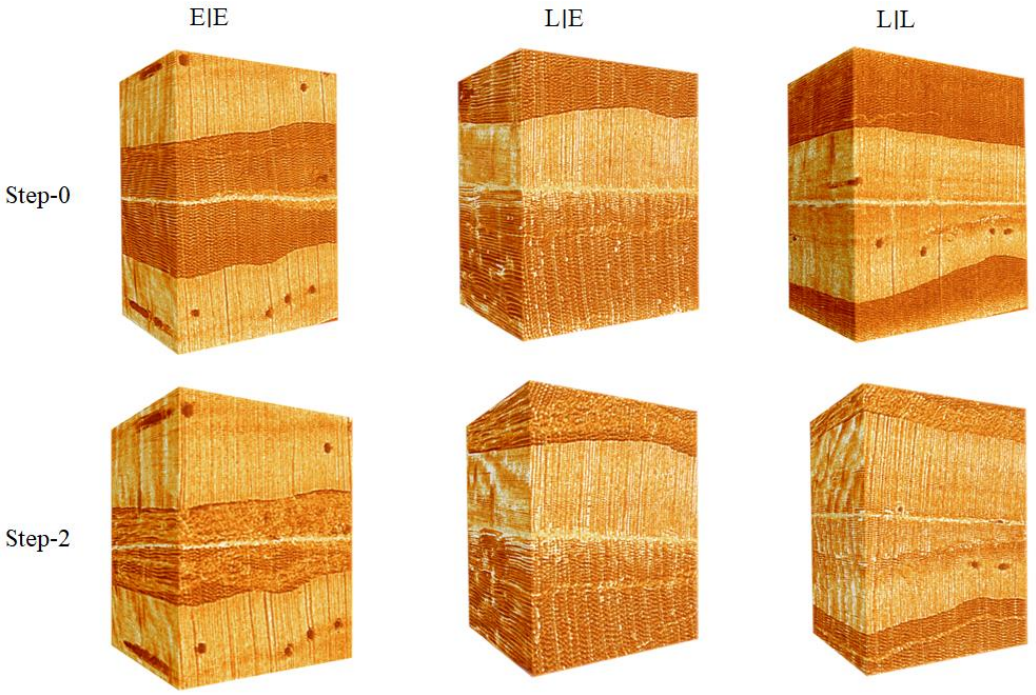

Fig.5. The 3D structure of three specimens at two compression steps. (E=earlywood, L=latewood)

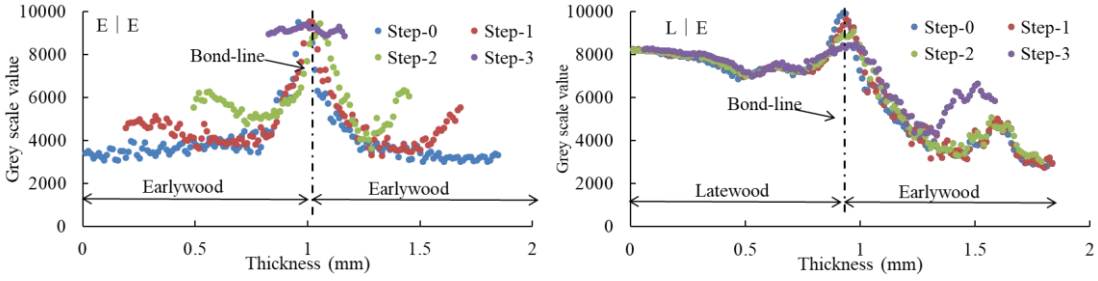

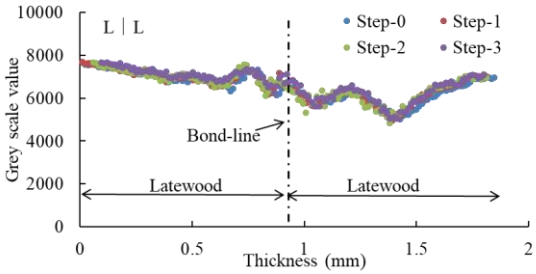

Fig.6. The grey-scale value distributions in ROIs of three specimens, at four compression steps. (E=earlywood, L=latewood)

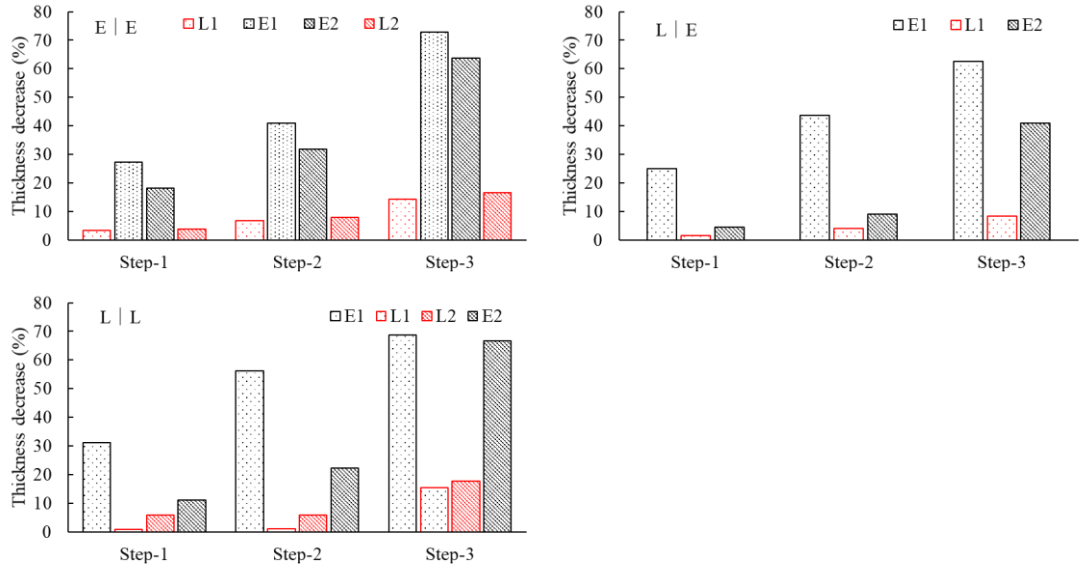

Fig.7. Decrease in thickness in each part of the three specimens at different compression steps. (E=earlywood, L=latewood)

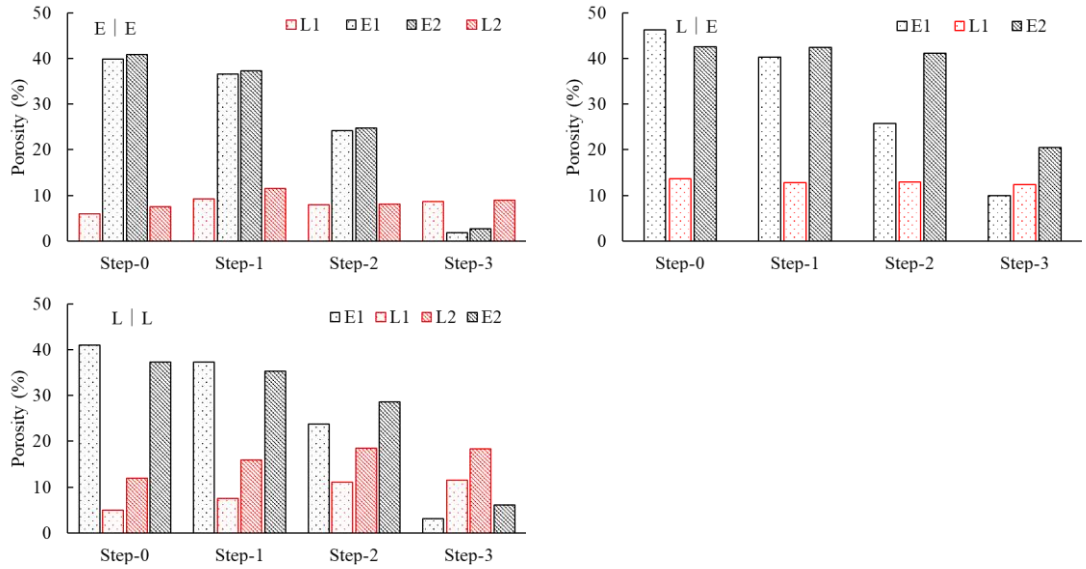

Fig.8. Porosity changes in each part of three specimens at different compression steps. (E=earlywood, L=latewood)

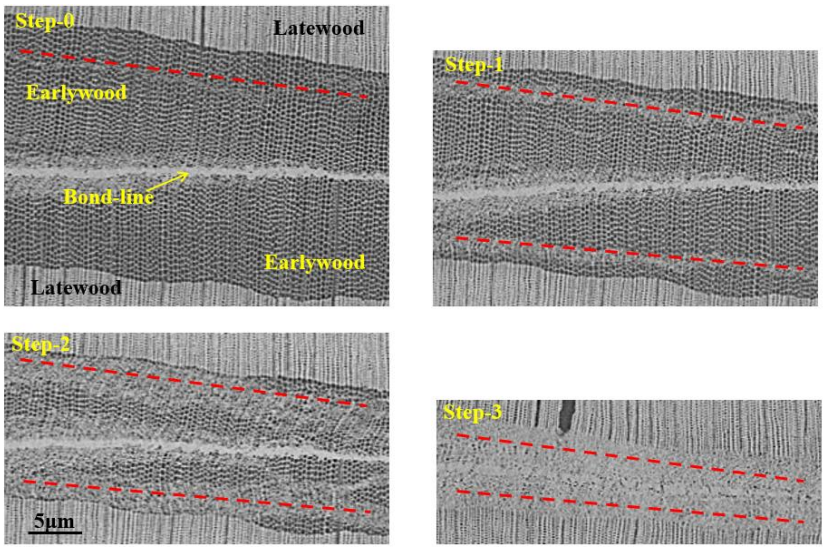

Fig.9. Meso-structural changes in the earlywood/earlywood (E|E) specimen, at four compression steps.

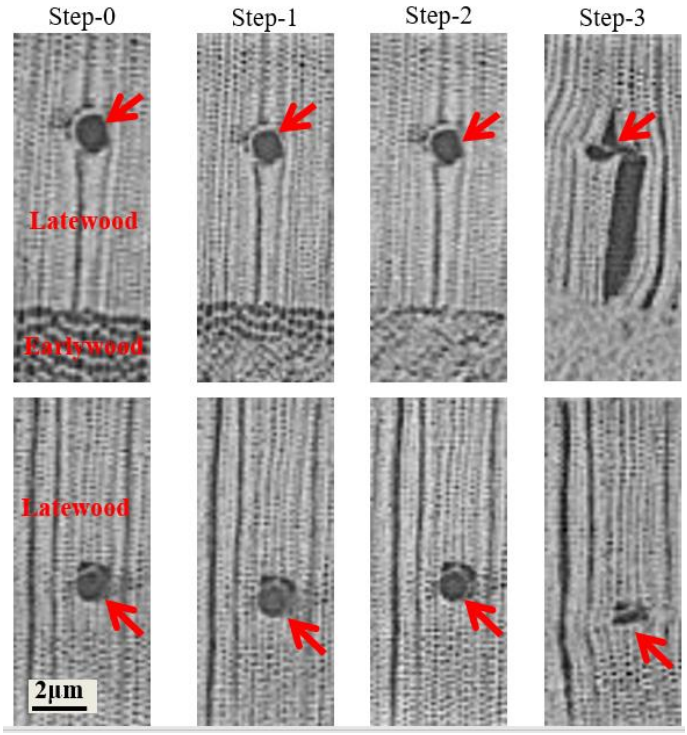

Fig.10. Micro-structural changes in earlywood/earlywood (E|E) specimen at four compression steps. Red arrows indicate resin ducts.

Table 1

Latewood and compressive strength of three specimens at different compression steps. (E=earlywood, L=latewood)

Types	E|E			L|E			L|L		
Latewood ratio (%)	58.8			24.3			53.7		
Compressive strength (N/mm^2)	Step-1	Step-2	Step-3	Step-1	Step-2	Step-3	Step-1	Step-2	Step-3
	5.20	5.38	27.26	5.30	5.56	9.81	5.50	6.81	18.88